ADVANCED MATERIALS
www.advmat.de

# Graphene–Vanadium Oxide Heterojunction Boosting Electron–Ion Coupling for Ultrahigh Energy Density Carbon Fiber Structural Supercapacitors

*Heng Zhou, Jing Wang, Laifa Shen,* Penghua Liang, Xin Xu, Boman Li, Zheng Zhang, Xingrong Zhu, Zhihan Kong, Jun Guo, Dingwei Ji, Longbiao Yu, Kang Yan, Linfeng Hu,* and Kongjun Zhu**

**The rapid advancement of drone logistics and electric aviation has created a growing demand for carbon fiber structural supercapacitors (CF–SSCs) that combine energy storage with lightweight and structural functionality. However, achieving high energy density remains challenging due to the chemical inertness of carbon fiber. In this work, it is demonstrated that $H_2V_3O_8$/rGO is a promising and high-performance electrode coating for carbon fiber structural supercapacitors that possess both ultrahigh energy density and load-bearing functionality. Herein, a simple and efficient one-step high-temperature mixing hydrothermal method is developed to synthesize $H_2V_3O_8$/rGO. Density functional theory calculations reveal that strong interfacial synergy between rGO and $H_2V_3O_8$ promotes electron transport and $Li^+$ diffusion, boosting efficient electron–ion coupling. The device exhibits high capacitance (964 mF $g^{-1}$) and exceptional energy density (502.1 mWh $kg^{-1}$), exceeding previously reported values. Remarkably, it maintains 88% capacitance retention after 5 000 cycles at 3 A $g^{-1}$ under a compressive load of 120 kPa, exceeding the 83% retention without load, demonstrating excellent electrochemical load-bearing stability. In addition, the device shows robust mechanical properties (127.2 MPa tensile strength, 6.95 GPa tensile modulus) and high safety, offering strong potential for practical application. This study proposes a promising strategy for designing CF–SSCs with high energy density.**

## 1. Introduction

With the rapid development of electric aircraft and unmanned aerial vehicles worldwide,[1] energy storage systems are subject to increasingly stringent requirements to achieve high energy density, low weight, and reliable structural load-bearing capability simultaneously.[2,3] In traditional power supply systems, structural components and energy storage units are physically and functionally separate. Structural components lack energy storage capability, and their considerable weight severely limits the overall energy density of the system. Energy storage units cannot bear mechanical loads and are susceptible to thermal runaway risks.[4] Therefore, structural energy storage technologies have gradually emerged.[5–9] Among these, CF–SSCs (Carbon Fiber Structural Supercapacitors) integrate carbon fiber (CF) electrodes with epoxy resin-based solid electrolytes, simultaneously provide mechanical load-bearing and energy storage capabilities.[10–12] This multifunctional design offers significant potential to replace conventional

H. Zhou, J. Wang, X. Xu, Z. Zhang, X. Zhu, Z. Kong, J. Guo, D. Ji, L. Yu, K. Yan, K. Zhu
State Key Laboratory of Mechanics and Control for Aerospace Structures, College of Aerospace Engineering
Nanjing University of Aeronautics and Astronautics
Nanjing 210016, China
E-mail: kjzhu@nuaa.edu.cn

H. Zhou, L. Shen, Z. Kong, D. Ji, L. Yu
College of Materials Science and Technology
Nanjing University of Aeronautics and Astronautics
Nanjing 210016, China
E-mail: lfshen@nuaa.edu.cn

P. Liang
Huzhou Key Laboratory of Green Energy Materials and Battery Cascade Utilization, School of Intelligent Manufacturing
Huzhou College
Huzhou 313000, China

B. Li
School of Chemistry and Chemical Engineering
Yangzhou University
Yangzhou 225002, China

L. Hu
School of Materials Science and Engineering
Southeast University
Nanjing 211189, China
E-mail: linfenghu@seu.edu.cn

The ORCID identification number(s) for the author(s) of this article can be found under https://doi.org/10.1002/adma.202514323

DOI: 10.1002/adma.202514323

 

structural components and enhance the overall energy density of the system.[13]

Carbon fibers (CFs) exhibit high strength,[14,15] low weight,[10] and good electrical conductivity.[16,17] However, their intrinsically low specific surface area and chemical inertness present major challenges for their use as electrodes, severely limiting their charge storage capacity.[18] Therefore, recent research has focused on modifying the CF surface by introducing various pseudocapacitive materials, including transition metal oxides[19–28] and conducting polymers.[29,30] Among these, metal oxides have become central to pseudocapacitor research due to their multiple valence states and high theoretical capacitance. For example, Sha et al.[31] reported a structural supercapacitor based on CF electrodes modified with vertical graphene (VG) and manganese dioxide ($MnO_2$), achieving an areal capacitance of 30.7 mF $cm^{-2}$. Deka et al.[32] developed a structural supercapacitor based on ZnO nanorods grown on CF fabric, which resulted in a significant increase in specific capacitance from 0.2 to 18.8 F $g^{-1}$. Pseudocapacitive CF–SSCs store charge through fast and reversible redox reactions and offer higher specific capacitance and energy density compared to electric double-layer CF–SSCs.[33–39] Therefore, the incorporation of pseudocapacitive mechanisms is widely recognized as a key strategy for enhancing the energy storage performance of CF–SSCs.

Among various metal oxides, $H_2V_3O_8$ is a layered hydrated vanadium oxide featuring a wide voltage window,[40] high specific capacitance,[41] and large interlayer spacing. The presence of both $V^{4+}$ and $V^{5+}$ oxidation states enables multiple redox reactions, making it an excellent pseudocapacitive material.[42] $H_2V_3O_8$ has demonstrated promising energy storage performance in aqueous supercapacitors[43] and secondary batteries.[44–46] However, its application in CF–SSCs remains unexplored, and further investigation is needed. Notably, $H_2V_3O_8$ still suffers from low electrical conductivity and structural instability caused by volume expansion during charge/discharge processes, resulting in poor rate capability and cycling stability. Incorporating conductive materials is an effective strategy to enhance the overall conductivity of the electrode. Hu et al.[43] developed a $V_3O_7{\cdot}H_2O$/CNT/rGO composite with a 3D porous structure via a one-step hydrothermal self-assembly strategy, exhibiting excellent specific capacitance and cycling stability (99.7% retention after 10 000 cycles) in aqueous supercapacitors. Liang et al.[47] synthesized $H_2V_3O_8$/MXene composite via a one-step high-temperature mixing hydrothermal method (HTMM), where interfacial electric field effects promoted $Zn^{2+}$ diffusion and enhanced pseudocapacitive reactions, enabling excellent performance at high rates and over long cycling periods. Reduced graphene oxide (rGO), a 2D material with high electrical conductivity and large surface area, has received increasing attention. Combining rGO with active materials can significantly improve their conductivity and enhance overall electrochemical performance.[48–50]

Here, we propose a simple and efficient one-step HTMM to synthesize $H_2V_3O_8$/rGO heterojunction. For the first time, a carbon fiber structural supercapacitor ($H_2V_3O_8$/rGO@CF–SSC) was fabricated using $H_2V_3O_8$/rGO as the electrode coating. The electrochemical performance, capacitance retention under load, mechanical tensile properties, and safety performance of $H_2V_3O_8$/rGO@CF–SSC were systematically investigated. Notably, the designed $H_2V_3O_8$/rGO@CF–SSC achieves ultrahigh energy density, which exceeds that of previously reported CF–SSCs. Furthermore, kinetic analysis and density functional theory (DFT) calculations reveal the underlying mechanism of the interfacial synergy between rGO and $H_2V_3O_8$ in enhancing electrochemical performance. This study fills the gap in vanadium oxide-based CF–SSCs, and provides a rational and effective approach to increase the energy density of CF–SSCs.

## 2. Results and Discussion

### 2.1. Characterization of Materials

$H_2V_3O_8$/rGO was synthesized via a simple and efficient one-step high-temperature mixing method, as illustrated in **Figure 1a**. Previous studies have demonstrated that this method effectively shortens the synthesis time and improves both the crystallinity and purity of the product.[51,52]The microstructure of $H_2V_3O_8$ and $H_2V_3O_8$/rGO was characterized by field-emission scanning electron microscopy (FE-SEM) and transmission electron microscopy (TEM). As shown in Figure 1b and Figure S1a (Supporting Information), pristine $H_2V_3O_8$ exhibits a densely stacked, regular nanorod morphology, suggesting that interactions during synthesis promote spontaneous stacking. The introduction of rGO mitigates excessive nanorod stacking, increases the exposure of active sites, and facilitates ion transport. TEM images (Figure 1c; Figure S1b, Supporting Information) further confirm that $H_2V_3O_8$ nanorods are in close contact with rGO flakes, forming a 3D conductive network with a well-defined heterojunction interface. The rGO provides high specific surface area and excellent electron conductivity, whereas $H_2V_3O_8$ contributes Faradaic charge storage as a pseudocapacitive material. The synergistic interaction between these components enhances electron transport and establishes a favorable interfacial environment for rapid Faradaic reactions.

The high-resolution transmission electron microscopy (HRTEM) image of $H_2V_3O_8$/rGO (Figure 1d) reveals lattice fringes with a spacing of 0.467 nm, corresponding to the (020) plane of $H_2V_3O_8$. Disordered regions attributable to rGO are also evident, confirming the coexistence of both phases within the composite. The selected–area electron diffraction (SAED) pattern (Figure 1e) displays distinct polycrystalline rings indexed to the (002), (210), and (011) planes, confirming the polycrystalline nature of $H_2V_3O_8$/rGO, which may facilitate multidirectional ion diffusion. The high-angle annular dark field (HAADF) image (Figure 1f) and the corresponding energy dispersive X-ray (EDX) elemental mapping (Figure 1g–i) further verify the uniform distribution of V on rGO, indicating the successful integration of $H_2V_3O_8$ nanorods with rGO sheets, which is beneficial for enhancing the electrochemical performance.

As shown in **Figure 2b**, the diffraction peaks of $H_2V_3O_8$/rGO are located at the same positions as those of $H_2V_3O_8$ nanorods, indicating that the crystal structure remains stable after compositing with rGO, without the formation of any impurity phases. This structural integrity preserves the layered framework composed of $VO_6$ octahedra and $VO_5$ trigonal bipyramids[52] (Figure 2a). Moreover, the presence of water molecules within the interlayer spacing acts as structural pillars, expanding the interlayer distance, which is essential for maintaining efficient $Li^+$

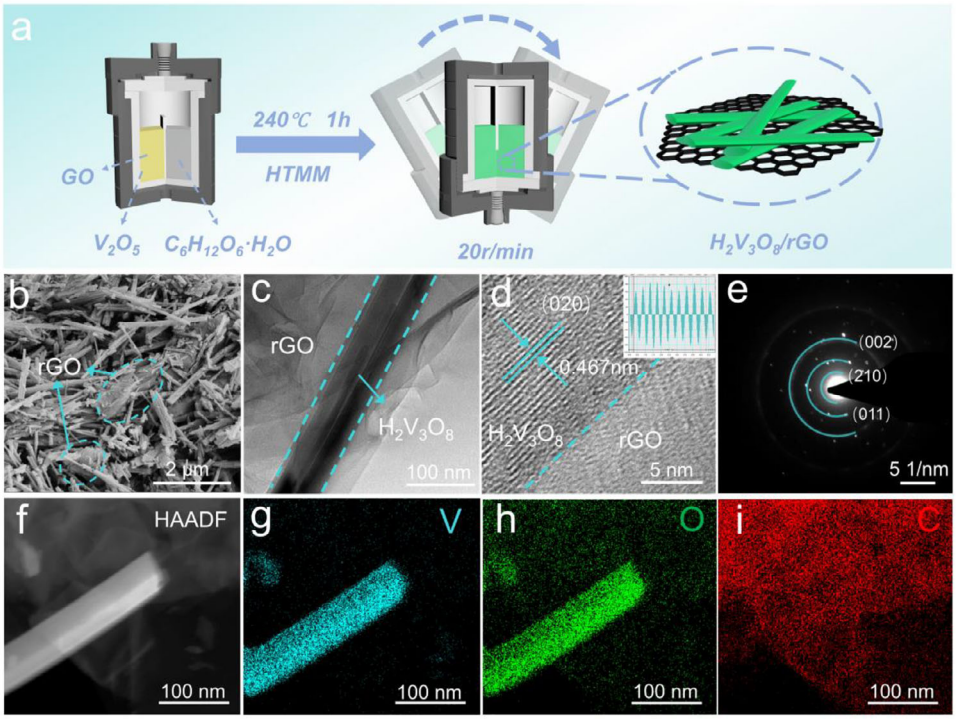


**Figure 1.** Morphology characterization of $H_2V_3O_8$/rGO: a) Schematic of the synthesis process for $H_2V_3O_8$/ rGO. b) FE-SEM image. c) TEM image. d) HRTEM image. e) SAED spectrum of $H_2V_3O_8$/rGO. f) HAADF image. g–i) Corresponding EDX mapping.

diffusion pathways along the layered structure. The Raman spectra of the samples provide further structural insight. As shown in Figure 2c, $H_2V_3O_8$ exhibits characteristic peaks at 139.4, 282.6, 405.8, 522, 688.4, 875.4, and 992.2 $cm^{-1}$, corresponding to its orthorhombic crystal structure. The peak at 139.4 $cm^{-1}$ is attributed to the stretching mode of $(V_2O_2)_n$ chains. Peaks at 282.6 and 405.8 $cm^{-1}$ are associated with the bending vibrations of V═O bonds, whereas those at 522.0, 688.4, and 875.4 $cm^{-1}$ correspond to the stretching vibrations of $V_3$—O and $V_2$—O bonds, respectively. The peak at 992.2 $cm^{-1}$ is related to the stretching vibration of terminal oxygen. These characteristic peaks remain present in $H_2V_3O_8$/rGO, indicating strong interaction between $H_2V_3O_8$ and rGO. Additionally, Figure S2 (Supporting Information) presents the Raman spectrum in the 1150–1650 $cm^{-1}$ range. $H_2V_3O_8$/rGO displays distinct D (≈1350 $cm^{-1}$) and G (≈1590 $cm^{-1}$) bands, typical of rGO. The D band originates from structural defects and disordered regions in graphene sheets, while the *G* band arises from the in-plane vibrations of $sp^2$ hybridized carbon atoms. The presence of both bands further confirms successful integration of rGO with $H_2V_3O_8$, indicating the formation of a composite structure with strong interfacial interaction.

The specific surface area was measured using nitrogen adsorption–desorption isotherms. As shown in Figure 2d and Figure S3 (Supporting Information), $H_2V_3O_8$/rGO exhibits a higher surface area (22.552 $m^2\ g^{-1}$) than $H_2V_3O_8$ (18.713 $m^2\ g^{-1}$) and is rich in mesopores. The increased surface area provides more electrochemically active sites and facilitates electrolyte penetration, promoting rapid $Li^+$ diffusion and enhancing charge storage performance.

The surface chemical composition and elemental valence states were analyzed by X–ray photoelectron spectroscopy (XPS). As shown in Figure 2e, the survey spectra reveal the presence of V, O, and C in both $H_2V_3O_8$ and $H_2V_3O_8$/rGO, with no additional elements detected. The high-resolution V 2p XPS spectrum (Figure 2f) confirms the coexistence of $V^{4+}$ and $V^{5+}$ oxidation states. This mixed-valence state promotes fast and reversible surface redox reactions, beneficial for enhancing pseudocapacitive performance. In the high-resolution O 1s spectrum (Figure 2g), the peaks at 530.1, 531.0, and 532.8 eV correspond to O—$V^{5+}$, HO—V, and O—$V^{4+}$ bonds, respectively.[53,54] The high-resolution C 1s spectrum (Figure S4, Supporting Information) displays three peaks attributed to C—C, C—O, and C—O functional groups.[55] These oxygen-containing functional groups may form hydrogen bonds or weak coordination interactions with $H_2V_3O_8$, improving interfacial contact and facilitating electronic coupling at the heterointerface.

### 2.2. Characterization of Electrochemical Performance

The preparation process for the epoxy resin-based electrolyte and the assembly flowchart for $H_2V_3O_8$/rGO@CF–SSC are shown in **Figure 3a**. To determine the optimal operating voltage window for $H_2V_3O_8$/rGO@CF–SSC, cyclic voltammetry (CV) tests were performed on $H_2V_3O_8$@CF–SSC across a voltage range of 1.5–2.5 V (Figure 3b). The CV curve at 2.0 V exhibits the most symmetric and stable shape, indicating high coulombic efficiency and minimal polarization during charge–discharge processes. As shown in Figure 3c, CV curves were recorded at various scan rates.

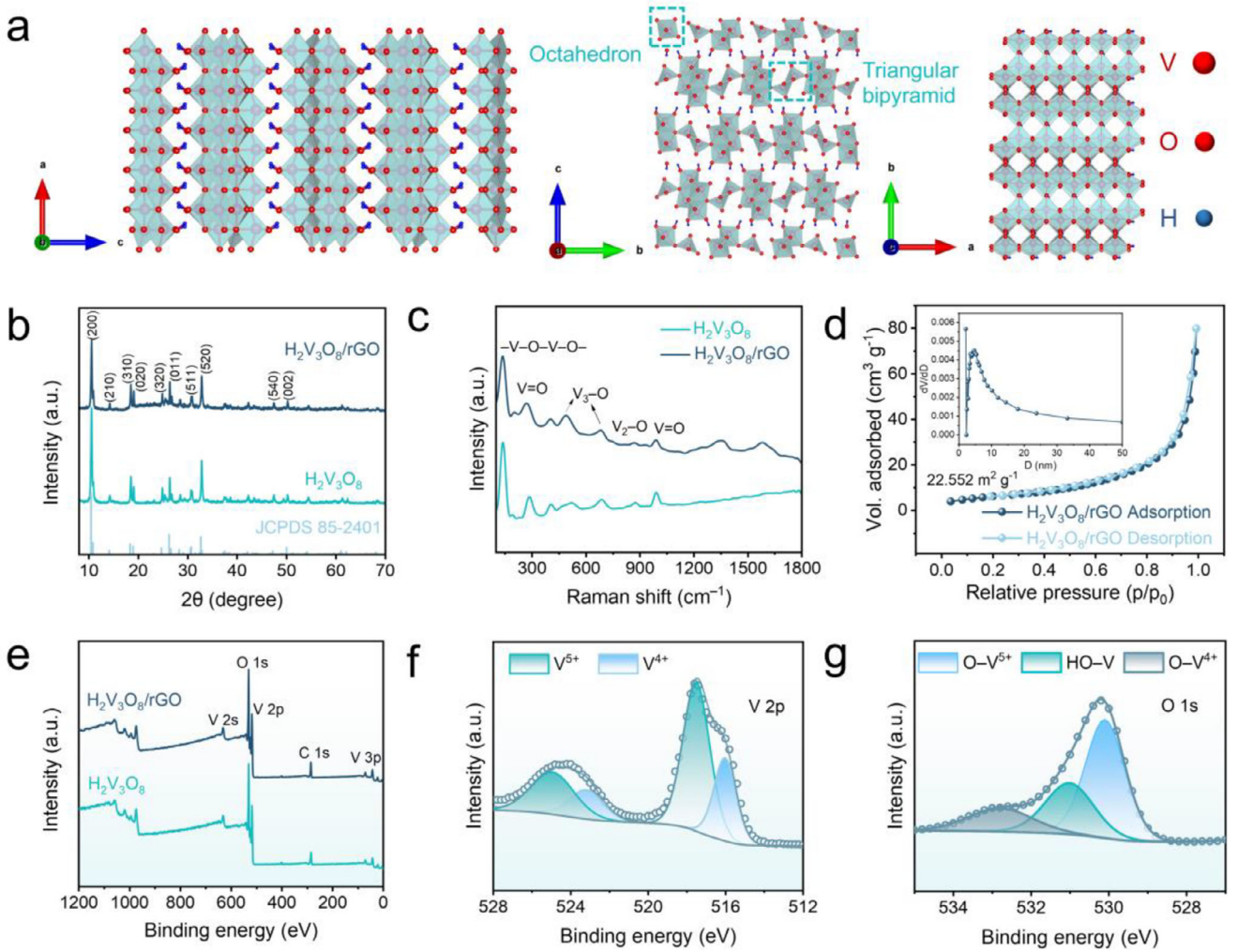


**Figure 2.** Structural characterization of $H_2V_3O_8$/rGO: a) Crystalline structure of $H_2V_3O_8$. b) XRD patterns. c) Raman spectra. d) $N_2$ adsorption–desorption isotherms and pore size distribution. e) XPS spectra. f–g) High-resolution XPS spectra of V and O in $H_2V_3O_8$/rGO.

At a low scan rate (10 mV $s^{-1}$), distinct redox peaks are observed, demonstrating the reversible redox behavior of $H_2V_3O_8$/rGO, which is characteristic of pseudocapacitive charge storage. As the scan rates (up to 100 mV $s^{-1}$), the redox peaks become less pronounced, but the curves remained nearly symmetric, suggesting fast and reversible charge transfer process. These results indicate that the energy storage mechanism in $H_2V_3O_8$/rGO@CF–SSC is primarily governed by surface-controlled pseudocapacitive behavior. The galvanostatic charge–discharge (GCD) profiles of $H_2V_3O_8$/rGO@CF–SSC at various current densities are presented in Figure 3d. At a current density of 0.1 A $g^{-1}$, the specific capacitance based on active material reaches 82 F $g^{-1}$ (964 mF $g^{-1}$, based on the total device mass), with a coulombic efficiency approaching 90%. Figure 3e summarizes the specific capacitance values at different current densities.

The effect of rGO on electrochemical performance is illustrated in Figure 3f,g. $H_2V_3O_8$/rGO@CF–SSC exhibits a significantly larger CV curve area and current response than $H_2V_3O_8$@CF–SSC at 10 mV $s^{-1}$. Similarly, higher specific capacitance is maintained at various current densities, consistent with the CV results. This enhancement is primarily attributed to the increased conductivity of rGO, which facilitates fast charge transfer. Cycling stability evaluated at 0.1 A $g^{-1}$(Figure S5, Supporting Information) shows that after ≈50 cycles, $H_2V_3O_8$/rGO@CF–SSC retains a specific capacitance of 74.6 F $g^{-1}$, notably higher than $H_2V_3O_8$@CF–SSC (48.6 F $g^{-1}$) and capacity retention is maintained at 88%, compared with only 61% for $H_2V_3O_8$@CF–SSC. At a high current density of 3 A $g^{-1}$, $H_2V_3O_8$/rGO@CF–SSC retained 83% of its capacity after 5000 cycles, outperforming $H_2V_3O_8$@CF–SSC, which retains 72% (Figure 3h). These results demonstrate that the rGO conductive network not only enhances specific capacitance but also mitigates volume expansion during cycling,[40,50] thereby substantially improving long–term cycling stability. Figure S6 (Supporting Information) presents the variation of energy density and power density for $H_2V_3O_8$/rGO@CF–SSC at different current densities. Based on the total mass of the device, the maximum power density reaches 11.34 W $kg^{-1}$, and the maximum energy density achieves 502.1 mWh $kg^{-1}$(0.502 Wh $kg^{-1}$, based on the total device mass), exceeding previously reported values (see Figure 3i; Table S1,

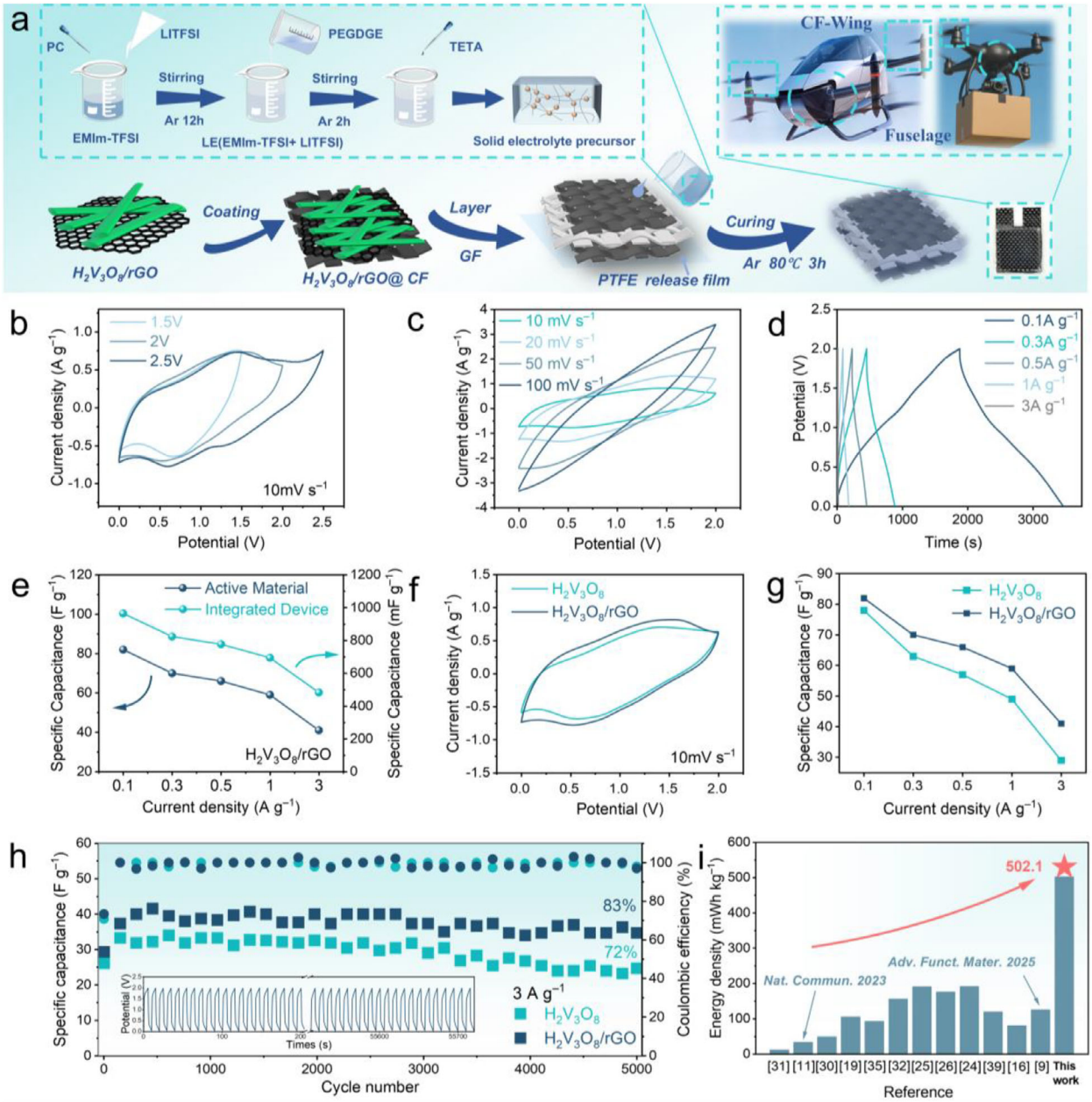


**Figure 3.** Electrochemical energy storage performances of $H_2V_3O_8$/rGO@CF–SSC: a) Preparation of epoxy resin–based electrolytes and assembly of $H_2V_3O_8$/rGO@CF–SSC. b) CV curves at different voltage windows for $H_2V_3O_8$@CF–SSC. c) CV curves at different scan rates. d) GCD curves at different current densities. e) Specific capacitance values at various current densities. f) CV curves (10 mV s$^{-1}$) and g) specific capacitance values for $H_2V_3O_8$@CF–SSC and $H_2V_3O_8$/rGO@CF–SSC. h) Cycling stability of $H_2V_3O_8$@CF–SSC and $H_2V_3O_8$/rGO@CF–SSC at 3 A g$^{-1}$. i) Energy density comparison between $H_2V_3O_8$/rGO@CF–SSC and previously reported values.

Supporting Information). These findings confirm the strong potential of $H_2V_3O_8$/rGO as a high-performance pseudocapacitive material for CF–SSCs.

### 2.3. Kinetic Analysis and DFT Calculations

The electrochemical reaction kinetics of $Li^+$ in $H_2V_3O_8$/rGO@CF–SSC was investigated, and the mechanism underlying the enhanced electrochemical performance resulting from rGO incorporation was further analyzed using DFT calculations. **Figure** 4a presents a schematic diagram of the charge–discharge process in $H_2V_3O_8$/rGO@CF–SSC. CV curves measured at scan rates from 1 to 20 mV s$^{-1}$. With increasing scan rates (Figure 4b; Figure S7, Supporting Information), the CV curves retain well-defined redox peaks, demonstrating a reversible $Li^+$ insertion/extraction process. The reduction peaks shifted toward lower potentials and the oxidation peaks

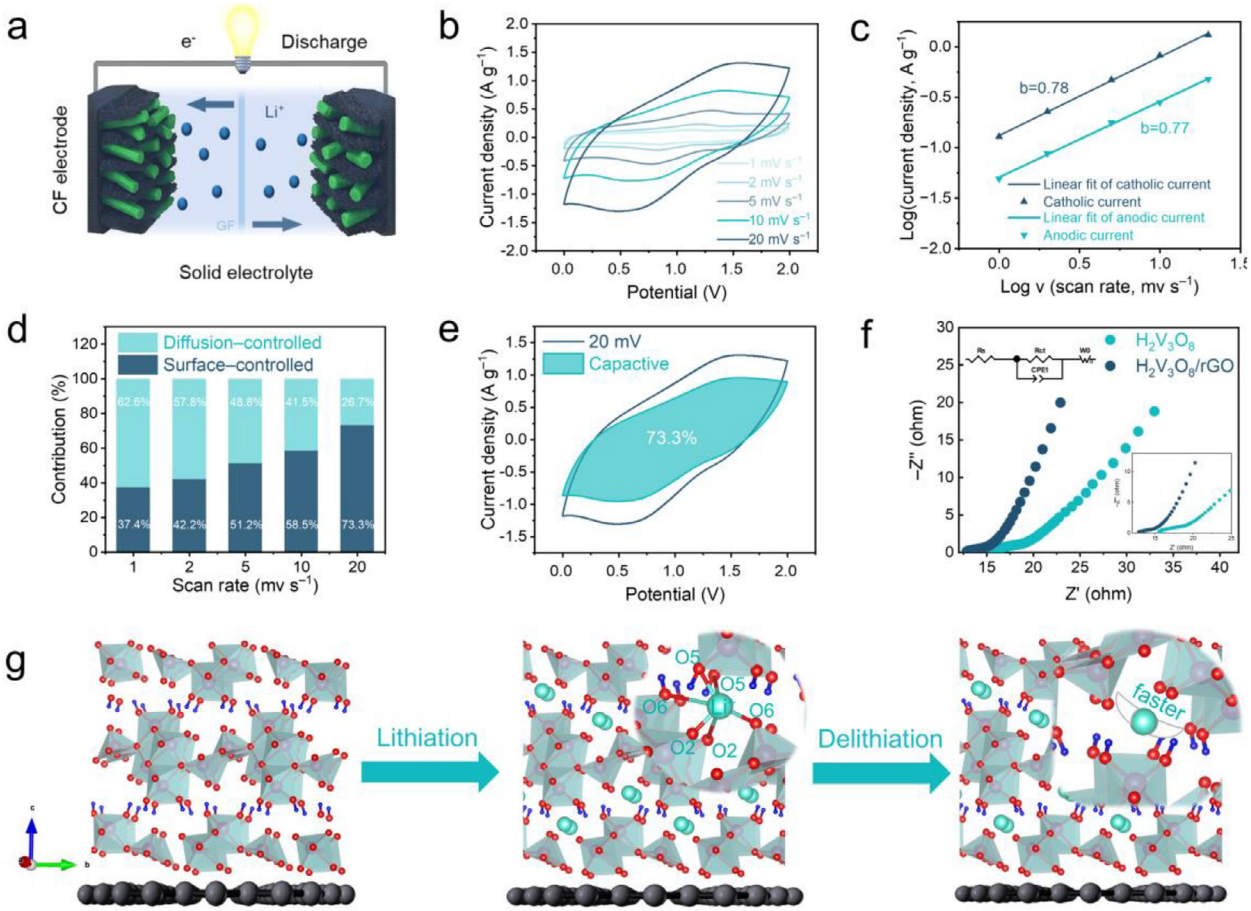


**Figure 4.** Kinetic analysis of $Li^+$ in $H_2V_3O_8$/rGO@CF–SSC: a) Schematic of the rechargeable. b) CV curves at various scan rates from 1 to 20 mV $s^{-1}$. c) Logarithmic relationship between peak current and scan rate. d–e) Capacitive and diffusion–limited contribution ratios. f) Nyquist plots. g) Schematic of reversible lithiation/delithiation.

toward higher potential with increasing scan rates, attributed to polarization caused by delayed electrode reaction response relative to the equilibrium potential.[52] To analyze the kinetics, the relationship between peak current ($i$) and scan rate ($v$) was evaluated using the power–law Equation (1):

$$i = av^b \tag{1}$$

where $a$ and $b$ are constants. A $b$-value approaching 0.5 indicates a diffusion–controlled process, while a value near 1 indicates a surface–controlled (capacitive) process.[56]

As shown in Figure 4c, the $b$ values for $H_2V_3O_8$/rGO@CF–SSC are 0.78 and 0.77, respectively, both higher than those for $H_2V_3O_8$@CF–SSC (Figure S8, Supporting Information), indicating faster electrochemical kinetics and a more surface–controlled reaction facilitated by the rGO network. The capacitive contribution to charge storage was further calculated using the Equation (2):

$$i\ (V) = k_1\, v + k_2 v^{\frac{1}{2}} \tag{2}$$

At each specific voltage, $k_1 v$ is the capacitance contribution and $k_2 v^{\frac{1}{2}}$ is the diffusion control contribution. As the scan rate increased from 1 to 20 mV $s^{-1}$, the capacitive contribution in $H_2V_3O_8$/rGO@CF–SSC increased from 37.4% to 73.3% (Figure 4d,e), whereas $H_2V_3O_8$@CF–SSC exhibited a lower increase (25.4% to 57.6%, Figure S9, Supporting Information), confirming that rGO enhances both electronic conductivity and $Li^+$ diffusion kinetics.

Electrochemical impedance spectroscopy (EIS) was used to assess the charge transfer and ion diffusion. Nyquist plots (Figure 4f) shows that the intrinsic resistance decreased from 15.5 to 12.85 Ω upon rGO addition. The reduced semicircle diameter, representing lower charge transfer resistance (Rct), further demonstrates improved interfacial charge transfer. In the low–frequency region, a steeper slope in $H_2V_3O_8$/rGO@CF–SSC confirms enhanced ion diffusion. Collectively, these kinetic analyses support the $Li^+$ insertion/extraction mechanism illustrated in Figure 4g. $Li^+$ ions are inserted into vacant interlayer sites between the $V_3O_8$ layers, coordinating with six oxygen atoms (O6, O8, two O2, and two O5) to form distorted $LiO_6$ octahedra. This intercalation ensures continuous ion transport within the layered framework, which can be represented as:

$$H_2V_3O_8 + xLi^+ + xe^- \leftrightarrow Li_xH_2V_3O_8 \tag{3}$$

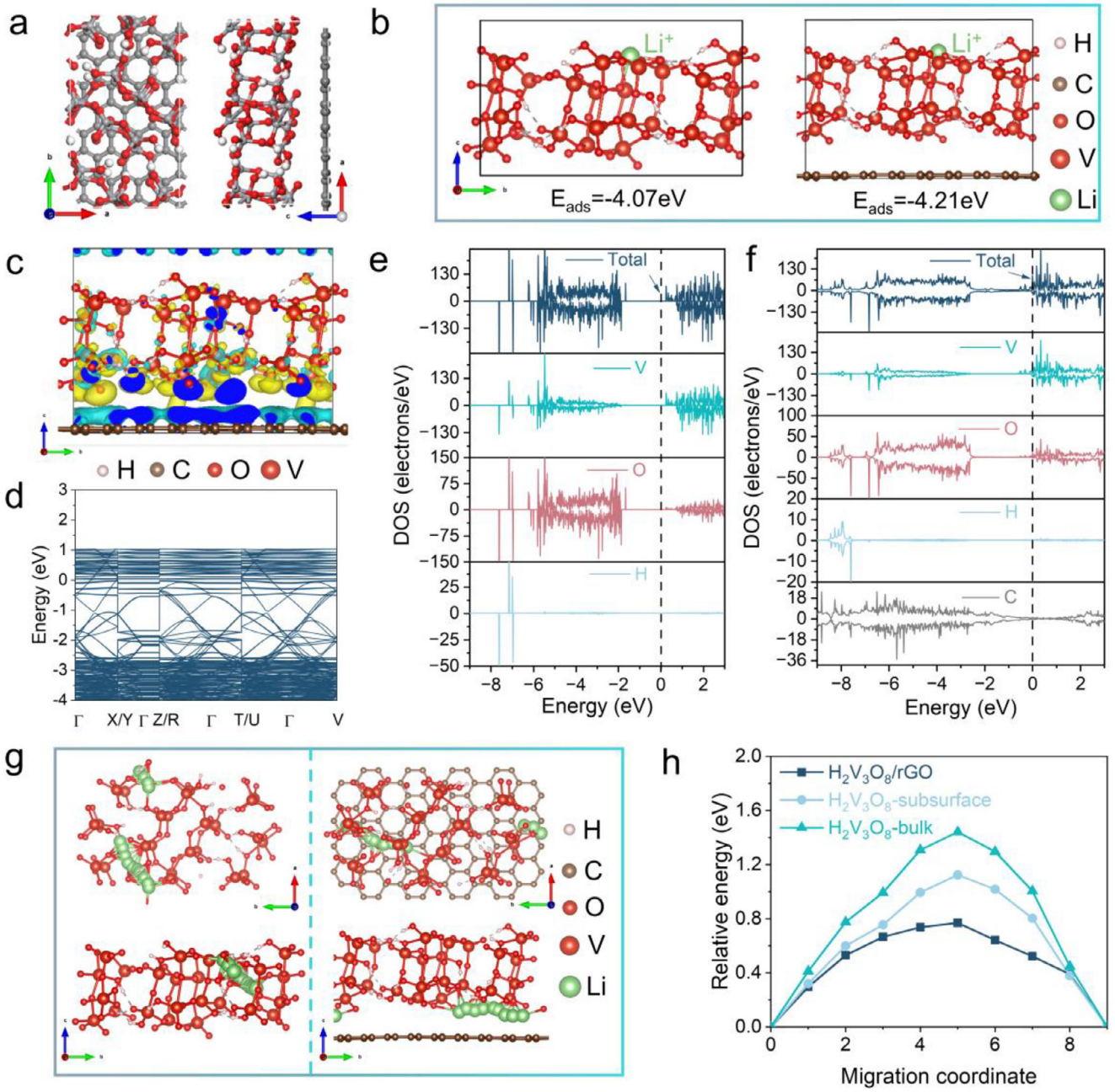


**Figure 5.** DFT calculations: a) Crystal structures of $H_2V_3O_8$/rGO. b) $Li^+$ adsorption configurations and energies. c) Electron difference density. d) Band structure. e) Density of state ($H_2V_3O_8$). f) Density of state ($H_2V_3O_8$/rGO). g) $Li^+$ diffusion pathway. h) Relative diffusion energy barriers for $Li^+$ in $H_2V_3O_8$ and $H_2V_3O_8$/rGO.

The incorporation of rGO enhances charge transport and ion diffusion, thereby boosting electron–ion coupling. This synergistic effect is the fundamental reason behind the excellent electrochemical performance of $H_2V_3O_8$/rGO@CF–SSC.

The mechanism by which rGO enhances electrochemical performance was further elucidated via DFT simulations. Computational models of $H_2V_3O_8$ and $H_2V_3O_8$/rGO are presented in Figure S10 (Supporting Information) and **Figure 5**a. To examine $Li^+$ adsorption, adsorption energies were calculated (Figure 5b). $Li^+$ exhibits a more negative adsorption energy in $H_2V_3O_8$/rGO, indicating greater adsorption stability. This stability arises from the introduction of rGO, which improves the electronic structure and provides additional active sites. This strengthens the interaction between $Li^+$ and surface oxygen atoms, facilitating the capture and accumulation of $Li^+$ at the interface. To assess interfacial charge transfer, the differential charge density distribution of $H_2V_3O_8$/rGO was calculated (Figure 5c). Yellow and blue regions indicate charge accumulation and depletion, respectively. Charge depletion on the rGO surface and accumulation near oxygen atoms confirm strong interfacial electronic

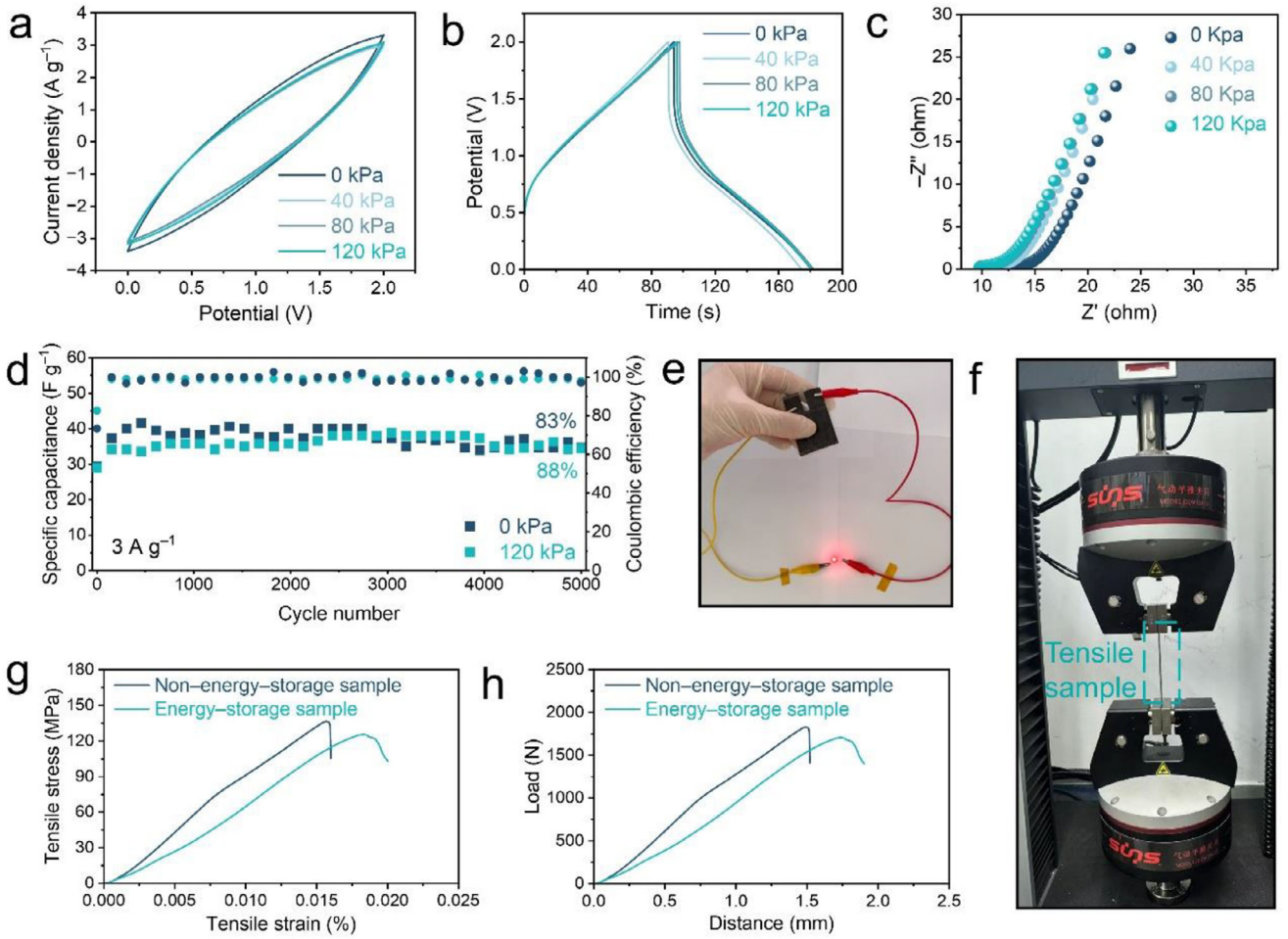


**Figure 6.** Electrochemical performance under 0, 40, 80, and 120 kPa surface loads and mechanical tensile test of $H_2V_3O_8$/rGO@CF–SSC: a) CV curves (100 mV $s^{-1}$), b) GCD curves (1 A $g^{-1}$), and c) EIS curves under different loads. d) Cycling stability under 0 and 120 kPa. e) Photograph of LED illumination. f) Schematic of tensile test. g) Stress–strain curves. h) Force-displacement curves.

interaction, which accelerate both electron transfer and ion diffusion.

Band structure calculations (Figure 5d; Figure S11, Supporting Information) reveal that the bandgap of $H_2V_3O_8$/rGO is significantly reduced relative to $H_2V_3O_8$, facilitating electron transition from the valence to conduction band and enhancing conductivity. Density of states (DOS) analysis further supports this (Figure 5e). $H_2V_3O_8$ displays a clear bandgap near the Fermi level (semiconducting), whereas $H_2V_3O_8$/rGO exhibits numerous states near the Fermi level (Figure 5f), consistent with metallic–like behavior. This improved electronic conductivity accelerates charge transport, and enhances the rate capability, as supported by the differential charge density analysis.

The effect of the heterointerface on $Li^+$ diffusion was evaluated using the climbing image nudged elastic band (CI—NEB) method. As shown in Figure 5h, the diffusion barriers for $Li^+$ in $H_2V_3O_8$ are 1.12 eV (subsurface diffusion within the interlayer channel) and 1.44 eV (bulk diffusion within the interlayer channel), while that in $H_2V_3O_8$/rGO is ≈0.76 eV, confirming that the incorporation of rGO effectively facilitates $Li^+$ diffusion. These results demonstrate that the $H_2V_3O_8$–rGO interface provides an effective pathway for accelerate $Li^+$ diffusion, and the improved diffusion kinetics substantially contribute to the enhanced rate performance,[57] consistent with EIS results. In summary, strong interfacial synergy between rGO and $H_2V_3O_8$ enhances electron transport and $Li^+$ diffusion, enabling efficient electron–ion coupling, and increasing $Li^+$ storage capacity, which collectively endow $H_2V_3O_8$/rGO@CF–SSC with outstanding electrochemical performance.

### 2.4. Electrochemical Performance Under Load and Mechanical Tensile Test

To realize an integrated structural and energy storage design, CF–SSCs must provide both energy storage capability and mechanical strength. The electrochemical performance of $H_2V_3O_8$/rGO@CF–SSC was evaluated under surface loads of 0, 40, 80, and 120 kPa to assess capacitance retention and cycling stability. As shown in **Figure 6a**, the CV curves at 100 mV $s^{-1}$ are nearly overlapping under all loads, with only a minor reduction in area after loading. GCD results (Figure 6b) demonstrate

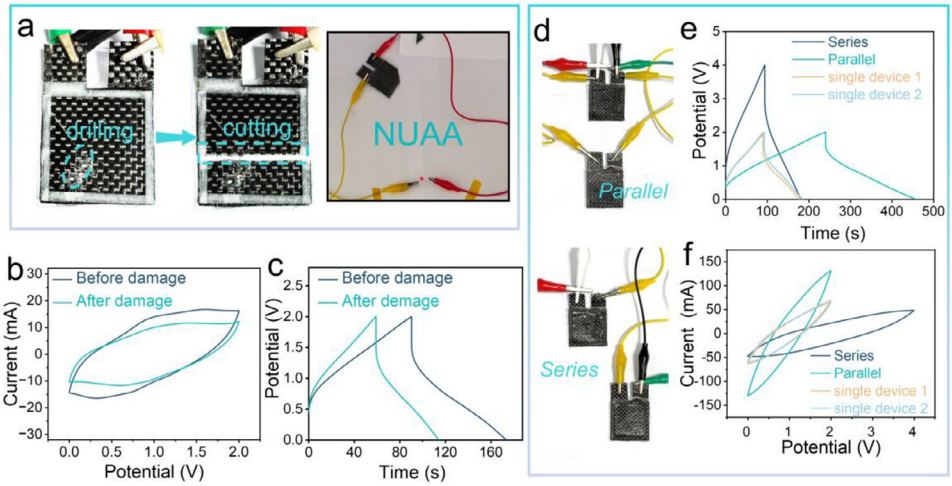


**Figure 7.** Electrochemical stability under structural damage of $H_2V_3O_8$/rGO@CF–SSC and performance in series/parallel configurations: a) Photograph of damaged device. b,c) CV (100 mV $s^{-1}$) and GCD (1 A $g^{-1}$) curves before and after damage. d) Photograph of series and parallel connection. e,f) CV (100 mV $s^{-1}$) and GCD (1 A $g^{-1}$) curves in series and parallel connection.

that at a current density of 1 A $g^{-1}$, the device retained 96.3% of its initial capacitance under a 120 kPa load, indicating excellent electrochemical stability under load, consistent with the CV results.

EIS measurements (Figure 6c) reveal that the internal resistance of $H_2V_3O_8$/rGO@CF–SSC decreases with increasing load, reflecting improved interfacial contact between the active material and CF substrate and more efficient electron transport pathways. However, a slight decline in specific capacitance is observed, likely due to compression of the electrode's porous structure during loading, which reduces electrolyte permeability and limits accessible active sites. These results suggest that while mechanical loading can improve interfacial conductivity, it may also impose compressive effects on the electrochemically active region. The cycling stability of $H_2V_3O_8$/rGO@CF–SSC under load was further assessed (Figure 6d). Following the application of a 120 kPa load, the device retained 88% of its capacitance after 5000 cycles at 3 A $g^{-1}$, higher than the 83% retention without loading. The applied load enhances contact between the electrode and current collector, lowers interface resistance, and improves electron transport. Furthermore, mechanical constraint helps stabilize the electrode structure, reducing degradation during repeated cycling and thus improving long-term cycling stability. The device could also reliably power an LED bulb after removal of load (Figure 6e). These results demonstrate not only excellent electrochemical load-bearing stability but also favorable mechano–electrochemical coupling performance, highlighting the potential of $H_2V_3O_8$/rGO@CF–SSC for structural energy storage integration in practical applications.

Mechanical tensile tests were performed using a standard strip specimen (150 mm × 20 mm × 0.7 mm) to evaluate the stress–strain behavior under mechanical stretching (Figure 6f). The mechanical properties of $H_2V_3O_8$/rGO@CF–SSC (energy–storage sample) and the non-energy-storage epoxy resin matrix composite ((CF/GF/CF)PEGDGE) were compared (Figure 6g,h). The non-energy-storage sample exhibits a linear stress–strain curve and brittle fracture, with a tensile strength of 136.2 MPa, and an elastic modulus of 8.68 GPa. In comparison, the energy–storage sample shows a tensile strength of 127.2 MPa and an elastic modulus of 6.95 GPa, representing reductions of only 7.1% and 20%, respectively, which may be attributed to the introduction of the conductive phase (EMIM–TFSI + PC + LiTFSI) into the electrolyte. Nevertheless, the mechanical strength and modulus of the energy-storage sample still exceed those of most previously reported systems (Table S2, Supporting Information). These findings indicate that $H_2V_3O_8$/rGO@CF–SSC provides excellent electrochemical energy storage while maintaining favorable mechanical properties, making it suitable for multifunctional composite applications requiring both strength and lightweight characteristics.

### 2.5. Electrochemical Stability Under Structural Damage and Device Configurability

Structural damage can critically affect the energy storage performance of CF–SSCs. To assess device resilience, $H_2V_3O_8$/rGO@CF–SSC was subjected to simultaneous cutting and drilling (**Figure 7a**). After the damage, CV and GCD measurements confirmed that the device retained a significant level of capacitance, with no short–circuit or malfunction detected (Figure 7b,c). At 1 A $g^{-1}$, the specific capacitance retention after damage is 68.5%, attributed to the loss of active material that no longer contributed to charge storage. Supporting video evidence (Video S1, Supporting Information) demonstrates that the device could still illuminate an LED after damage, further verifying its safety and operability. Unlike liquid electrolytes, the solid electrolyte employed here provides higher mechanical strength, maintaining separation between CF electrodes and preventing short-circuiting or electrolyte leakage upon piercing or cutting. These results confirm that the device remains functional and safe even when structurally damaged.

The practical applicability and integration potential of $H_2V_3O_8$/rGO@CF–SSC were further demonstrated by

evaluating its electrochemical performance in series and parallel configurations. As shown in Figure 7d, two devices connected in parallel and in series, and their GCD curves (Figure 7e) reveal higher voltage output for the series connection and higher current response for the parallel configuration, as expected for supercapacitor modules. The corresponding CV curves (Figure 7f) show an expanded voltage window for the series configuration and increased current for the parallel configuration, demonstrating excellent scalability and integration capacity. These results suggest that $H_2V_3O_8$/rGO@CF–SSC can be flexibly assembled to meet diverse energy requirements, providing a strong foundation for the development of stacked or multilayer structural energy storage systems for real–world applications.

## 3. Conclusion

In summary, a CF–SSC with ultrahigh energy density was designed using a simple and efficient one-step HTMM to synthesize the pseudocapacitive material $H_2V_3O_8$/rGO as the electrode coating. The interfacial synergy between the highly conductive rGO and the pseudocapacitive $H_2V_3O_8$ effectively enhances electron–ion coupling, facilitating charge transfer and ion diffusion. The assembled $H_2V_3O_8$/rGO@CF–SSC exhibits an exceptionally high specific capacitance (964 mF $g^{-1}$ at 0.1 A $g^{-1}$) and ultrahigh energy density (502.1 mWh $kg^{-1}$), exceeding previously reported CF–SSCs. Additionally, the device demonstrates excellent electrochemical load-bearing stability, retaining 88% of its capacitance after 5000 cycles under a compressive stress of 120 kPa. The device also exhibits outstanding mechanical properties, including a tensile strength of 127.2 MPa and a tensile modulus of 6.95 GPa, as well as high safety and application potential. This work fills the gap in vanadium oxide-based CF–SSCs and provides valuable insights into the design for CF–SSCs with high energy density.

## 4. Experimental Section

*Synthesis of $H_2V_3O_8$/rGO*: Graphene oxide (GO) was prepared following a previously reported method.[58] As shown in Figure 1a, 0.436 g of vanadium pentoxide ($V_2O_5$) and 20 mg of GO were dispersed in 12 mL of deionized water by ultrasonication for 1 h, then transferred to one side of a Teflon–lined multi–chamber autoclave. Separately, 0.048 g of glucose monohydrate was dissolved in another 12 mL of deionized water and added to the opposite side of the autoclave (total volume 70 mL). The reaction mixture was heated to 240 °C, and the rotating Teflon–lined autoclave enabled thorough mixing from both sides, allowing the reaction to proceed for 1 h. The resulting product was collected by vacuum filtration and dried under vacuum at 80 °C for 12 h to obtain a dark green powder. For comparison, pure $H_2V_3O_8$ nanorods were synthesized using the same high-temperature mixed hydrothermal process without the addition of GO.

*Preparation of $H_2V_3O_8$/rGO@CF and Epoxy Resin-Based Electrolyte Solution*: CF was soaked in a 1.85 mol $L^{-1}$ potassium hydroxide (KOH) solution for 12 h to remove surface adhesives and impurities, then rinsed thoroughly with deionized water to eliminate residual KOH.[3] The CF was vacuum–dried for 12 h. Active materials, acetylene black, and polyvinylidene fluoride (PVDF) were mixed in a mass ratio of 7:2:1 in N–methylpyrrolidone (NMP) to form a homogeneous slurry. This slurry was uniformly coated onto the CF and vacuum–dried at 80 °C for at least 10 h to obtain the $H_2V_3O_8$/rGO carbon fiber electrode ($H_2V_3O_8$/rGO@CF). Each electrode measured 35 mm × 35 mm, with a 15 mm × 12 mm region reserved as a current collector for connection to the electrochemical workstation.

To prepare the electrolyte, 5.9 g of EMIM–TFSI, 2.6 g of LiTFSI, and 0.06 g of propylene carbonate (PC) were mixed and stirred under argon in a glovebox for 12 h.[11] Then, 4 g of this mixture was combined with 2.38 g of PEGDGE and stirred for 1 h. TETA was slowly added as a crosslinking agent to yield the epoxy resin-based electrolyte solution.

*Fabrication of $H_2V_3O_8$/rGO@CF–SSC*: As shown in Figure 3a, the structural supercapacitor was prepared using a manual layering technique. Glass fiber (GF) was cut into a 40 mm × 40 mm square to separate the upper and lower electrodes. Both the positive and negative electrodes were $H_2V_3O_8$/rGO@CF. The fabrication was thoroughly cast with the epoxy resin-based electrolyte solution by pouring, then cured at 80 °C for 3 h under the coverage of a PTFE film in vacuum.

*Electrochemical and Mechanical Measurements*: Electrochemical tests were performed using a two-electrode setup with a CHI660 electrochemical workstation, employing CV, EIS, and GCD tests were conducted under open-circuit voltage conditions. The specific capacitance $C_g$ of the active material was calculated using the following Equation (4):

$$C_g = \frac{I \times t}{\Delta V \times m} \tag{4}$$

where $I$ is the discharge current (A), $t$ is the discharge time (s), $\Delta V$ is the voltage window (maximum voltage minus voltage drop), and $m$ is the mass (g) of the active material.

The energy density $E_g$ (mWh $kg^{-1}$) and power density $P_g$ (W $kg^{-1}$) of the $H_2V_3O_8$/rGO@CF–SSC were calculated based on the total mass of the device rather than the active materials. The specific formulas are as follows:

$$E_g = \frac{C_g \frac{m}{M} \times (\Delta V)^2}{2 \times 3.6} \tag{5}$$

$$P_g = \frac{3600 \times E_g}{t} \tag{6}$$

here, $M$ is the total mass of the device, which includes the CF electrode, electrolyte, and GF separator.

Mechanical properties were evaluated using a tensile testing machine (model JDQW104.00, SANS). Specimens used for tensile testing measured 150 mm × 20 mm × 0.7 mm. Tensile strength ($\sigma$, MPa) and Young's modulus ($E$, GPa) are as follows:

$$\sigma = \frac{F_{max}}{A} \tag{7}$$

$$E = \frac{\Delta\sigma}{\Delta\epsilon} = \frac{(F_2 - F_1)/A}{(L_2 - L_1)/L_0} \tag{8}$$

where $F_{max}$ is maximum applied force before fracture (N), $A$ is cross–sectional area of the specimen ($mm^2$), $F_1$ and $F_2$ are forces (N) within the linear elastic region, $L_1$ and $L_2$ are the specimen lengths (mm) under $F_1$ and $F_2$, respectively, and $L_0$ is the original gauge length (mm).

## Supporting Information

Supporting Information is available from the Wiley Online Library or from the author.

## Acknowledgements

H.Z. and J.W. contributed equally to this work. This work was financially supported by the National Natural Science Foundation of China (Grant

Nos. 52372200, 52171203, 52371214), the National Key Research and Development Program of China (Grant No. 2021YFB2400400), the Frontier Technologies R&D Program of Jiangsu (Grant No. BF2024033), the Research Fund of State Key Laboratory of Mechanics and Control for Aerospace Structure (Nanjing University of Aeronautics and astronautics) (Grant No. MCAS-E-0325G02).

## Conflict of Interest

The authors declare no conflict of interest.

## Data Availability Statement

The data that support the findings of this study are available from the corresponding author upon reasonable request.

## Keywords

electrochemical load-bearing stability, electron–ion coupling, energy density, $H_2V_3O_8$/rGO, structural supercapacitor

Received: July 25, 2025
Revised: September 17, 2025
Published online:

[1] A. W. Schäfer, S. R. Barrett, K. Doyme, L. M. Dray, A. R. Gnadt, R. Self, A. O'Sullivan, A. P. Synodinos, A. J. J. N. E. Torija, *Nat. Energy* **2019**, *4*, 160.
[2] E. S. Greenhalgh, S. Nguyen, M. Valkova, N. Shirshova, M. S. P. Shaffer, A. R. J. Kucernak, *Compos. Sci. Technol.* **2023**, *235*, 109968.
[3] Y. Xu, W. Lu, G. Xu, T.-W. Chou, *Compos. Sci. Technol.* **2021**, *204*, 108636.
[4] J. Fan, C. Liu, N. Li, L. Yang, X.-G. Yang, B. Dou, S. Hou, X. Feng, H. Jiang, H. Li, W.-L. Song, L. Sun, H.-S. Chen, H. Gao, D. Fang, *Nature* **2025**, *641*, 639.
[5] Y. Zhou, H. Qi, J. Yang, Z. Bo, F. Huang, M. S. Islam, X. Lu, L. Dai, R. Amal, C. H. J. E. Wang, *Energy Environ. Sci.* **2021**, *14*, 1854.
[6] R. Chaudhary, J. Xu, Z. Xia, L. E. Asp, *Adv. Mater.* **2024**, *36*, 2409725.
[7] C. Wang, Y. Zhang, M. Liao, P. Li, L. Ma, H. Yao, J. Qu, K. Zhang, C. Li, T. Song, Z. Yang, X. Gong, H. Jiang, C. Tang, J. Feng, X. Cheng, Y. Jiang, L. Ye, W. Li, D. Chao, H. Peng, B. Wang, *Adv. Mater.* **2025**, *37*, 2417662.
[8] L. E. Asp, E. S. Greenhalgh, *Compos. Sci. Technol.* **2014**, *101*, 41.
[9] Z. Zhang, L. Shen, X. Xu, Y. Liu, T. Xia, Z. Zhu, J. Xu, J. Wang, Q. Wu, K. Yan, J. Liu, H. Dong, K. Zhu, *Adv. Funct. Mater.* **2025**, https://doi.org/10.1002/adfm.202511334.
[10] J. Zhang, G. Lin, U. Vaidya, H. Wang, *Composites Part B-Engineering* **2023**, *250*, 110463.
[11] J. Zhang, J. Yan, Y. Zhao, Q. Zhou, Y. Ma, Y. Zi, A. Zhou, S. Lin, L. Liao, X. J. N. C. Hu, *Nat. Commun.* **2023**, *14*, 64.
[12] H. Zhou, H. Li, L. Li, T. Liu, G. Chen, Y. Zhu, L. Zhou, H. Huang, *Mater. Today Energy* **2022**, *24*, 100924.
[13] L. Yao, K. Zheng, N. Koripally, N. Eedugurala, J. D. Azoulay, X. Zhang, T. N. Ng, *Sci. Adv.* **2023**, *9*, adh0069.
[14] H. G. Chae, B. A. Newcomb, P. V. Gulgunje, Y. Liu, K. K. Gupta, M. G. Kamath, K. M. Lyons, S. Ghoshal, C. Pramanik, L. Giannuzzi, K. Şahin, I. Chasiotis, S. Kumar, *Carbon* **2015**, *93*, 81.
[15] M. Sharma, S. Gao, E. Mäder, H. Sharma, L. Y. Wei, J. Bijwe, *Compos. Sci. Technol.* **2014**, *102*, 35.
[16] S. H. Chen, L. Qiu, H. M. Cheng, *Chem. Rev.* **2020**, *120*, 2811.
[17] N. Forintos, T. Czigany, *Composites Part B-Engineering* **2019**, *162*, 331.
[18] Y. Zheng, W. Zhang, X. Zhu, F. Liu, C. Yang, W. Zheng, *J. Am. Chem. Soc.* **2024**, *146*, 20291.
[19] B. K. Deka, A. Hazarika, J. Kim, Y.-B. Park, H. W. Park, *Composites, Part A* **2016**, *87*, 256.
[20] A. González, E. Goikolea, J. A. Barrena, R. Mysyk, *Renew. Sustain. Energy Rev.* **2016**, *58*, 1189.
[21] Y. Duan, L. Wei, C. Cai, J. Mi, F. Cao, J. Chen, X. Li, X. Pang, B. Li, L. Wang, *Nano Res.* **2024**, *17*, 4764.
[22] Y. Song, T.-Y. Liu, B. Yao, T.-Y. Kou, D.-Y. Feng, X.-X. Liu, Y. Li, *Small* **2017**, *13*, 1700067.
[23] K. Subhani, N. Hameed, A. Al-Qatatsheh, J. Ince, P. J. Mahon, A. Lau, N. V. Salim, *J. Energy Storage* **2022**, *56*, 105936.
[24] B. K. Deka, A. Hazarika, J. Kim, N. Kim, H. E. Jeong, Y.-B. Park, H. W. Park, *Chem. Eng. J.* **2019**, *355*, 551.
[25] H. Zhou, A. Duongthipthewa, J. Zhang, H. Li, L. Peng, Y. Fu, H. Huang, L. Zhou, *Compos. Sci. Technol.* **2023**, *240*, 110068.
[26] H. D. Roh, B. K. Deka, H. W. Park, Y.-B. Park, *Compos. Sci. Technol.* **2021**, *213*, 108833.
[27] Y. Zhao, H. Xu, G. Cai, C. Yan, D. Liu, G. Chen, Y. Zhu, *Polym. Compos.* **2022**, *43*, 8458.
[28] O. Kwon, B. K. Deka, J. Kim, H. W. Park, *Int. J. Energy Res.* **2018**, *42*, 490.
[29] O. Hubert, N. Todorovic, L. M. Rojas González, E. Costagliola, A. Blocher, A. Mautner, R. T. Woodward, A. Bismarck, *Compos. Sci. Technol.* **2023**, *242*, 110152.
[30] A. Javaid, O. Khalid, A. Shakeel, S. Noreen, *J. Energy Storage* **2021**, *33*, 102168.
[31] Z. Sha, F. Huang, Y. Zhou, J. Zhang, S. Wu, J. Chen, S. A. Brown, S. Peng, Z. Han, C.-H. Wang, *Compos. Sci. Technol.* **2021**, *201*, 108568.
[32] B. K. Deka, A. Hazarika, O. Kwon, D. Kim, Y.-B. Park, H. W. Park, *Chem. Eng. J.* **2017**, *325*, 672.
[33] S. Fleischmann, J. B. Mitchell, R. Wang, C. Zhan, D.-e. Jiang, V. Presser, V. Augustyn, *Chem. Rev.* **2020**, *120*, 6738.
[34] X. Chen, R. Paul, L. Dai, *Natl. Sci. Rev.* **2017**, *4*, 453.
[35] M. F. Pernice, G. Qi, E. Senokos, D. B. Anthony, S. Nguyen, M. Valkova, E. S. Greenhalgh, M. S. P. Shaffer, A. R. J. Kucernak, *Multifunct. Mater.* **2022**, *5*, 025002.
[36] E. Senokos, Y. Ou, J. J. Torres, F. Sket, C. González, R. Marcilla, J. J. Vilatela, *Sci. Rep.* **2018**, *8*, 3407.
[37] Z. Zhang, L. Shen, X. Xu, Y. Liu, T. Xia, Z. Zhu, J. Xu, J. Wang, Q. Wu, K. Yan, J. Liu, H. Dong, K. Zhu, *ACS Appl. Energy Mater.* **2025**, *8*, 2485.
[38] K. Subhani, X. Jin, P. J. Mahon, A. Kin Tak Lau, N. V. Salim, *Composites Commun.* **2021**, *24*, 100663.
[39] A. Javaid, K. Ho, A. Bismarck, J. Steinke, M. Shaffer, E. Greenhalgh, *J. Compos. Mater.* **2018**, *52*, 3085.
[40] C. Liu, W. Xu, C. Mei, M.-C. Li, X. Xu, Q. Wu, *Chem. Eng. J.* **2021**, *405*, 126737.
[41] Q. Pang, C. Sun, Y. Yu, K. Zhao, Z. Zhang, P. M. Voyles, G. Chen, Y. Wei, X. Wang, *Adv. Energy Mater.* **2018**, *8*, 1800144.
[42] D. Chen, M. Lu, B. Wang, H. Cheng, H. Yang, D. Cai, W. Han, H. J. Fan, *Nano Energy* **2021**, *83*, 105835.
[43] T. Hu, Y. Liu, Y. Zhang, M. Chen, J. Zheng, J. Tang, C. Meng, *J. Colloid Inter. Sci.* **2018**, *531*, 382.
[44] D. Zhang, J. Cao, C. Yang, K. Lolupiman, W. Limphirat, X. Wu, X. Zhang, J. Qin, Y. Huang, *Adv. Energy Mater.* **2025**, *15*, 2404026.
[45] Y. Liu, X. Wang, Z.-S. Wu, Y.-R. Cho, X. Wu, *Adv. Funct. Mater.* **2025**, https://doi.org/10.1002/adfm.202505535.
[46] M. Zhang, X. Zhang, Q. Dong, S. Zhang, Z. Xu, Z. Hou, Y. Qian, *Adv. Funct. Mater.* **2023**, *33*, 2213187.
[47] P. Liang, T. Xu, K. Zhu, Y. Rao, H. Zheng, M. Wu, J. Chen, J. Liu, K. Yan, J. Wang, R. Zhang, *Energy Storage Mater.* **2022**, *50*, 63.
[48] Z. Ji, L. Chen, G. Tang, J. Zhong, A. Yuan, G. Zhu, X. Shen, *Small* **2024**, *20*, 2306236.

[49] A. Zhang, P. Ran, X. Han, S. Ke, A. Qiu, Z. Zhang, Y. Lv, M. Ding, J.-L. Zuo, *J. Mater. Chem. A* **2024**, *12*, 22037.
[50] Z. Li, Y. Xu, L. Wu, J. Cui, H. Dou, X. Zhang, *Nat. Commun.* **2023**, *14*, 6816.
[51] P. Liu, Y. Xu, K. Zhu, K. Bian, J. Wang, X. Sun, Y. Gao, H. Luo, L. Lu, J. Liu, *J. Mater. Chem. A* **2017**, *5*, 8307.
[52] P. Liu, K. Bian, K. Zhu, Y. Xu, Y. Gao, H. Luo, L. Lu, J. Wang, J. Liu, G. Tai, *ACS Appl. Mater. Inter.* **2017**, *9*, 17002.
[53] Y. Liu, Y. Sun, J. Zhang, X. Hao, M. Zhang, P. Wei, X. Zhao, K. Cai, *Nano Energy* **2024**, *120*, 109152.
[54] Y. Fang, C. Qi, W. Bao, F. Xu, W. Sun, B. Liu, X. Yu, L. Wang, W. Jiang, P. J. E. Qiu, *Energy Environ. Sci.* **2025**, *18*, 367.
[55] Z. Gan, X. Ren, M. Liu, N. Wang, T. Pian, M. Sun, C. Jia, Z. Li, *Chem. Eng. J.* **2025**, *506*, 160013.
[56] S. Huang, S. He, H. Qin, X. Hou, *ACS Appl. Mater. Interfaces* **2021**, *13*, 44379.
[57] X. Wang, S. Zhang, Y. Shan, L. Chen, G. Gao, X. Zhu, B. Cao, X. He, *Energy Storage Mater.* **2021**, *37*, 55.
[58] L. Yu, R. Zhang, R. Jia, W. Fa, H. Yin, L. Y. Zhang, H. Li, B. Xu, *J. Colloid Inter. Sci.* **2024**, *653*, 359.